Available online at www.sciencedirect.com
ScienceDirect
Advances in Space Research xxx (2010) xxx–xxx
ADVANCES IN SPACE RESEARCH (a COSPAR publication)
www.elsevier.com/locate/asr

Optimal combination of InSAR and GPS for measuring interseismic crustal deformation

Meng Wei [a,*], David Sandwell [a], Bridget Smith-Konter [b]

[a] Scripps Institution of Oceanography, University of California San Diego, 9500 Gilman Dr., La Jolla, CA 92093-0225, USA
[b] Department of Geological Science, University of Texas at El Paso, EL Paso, TX 79912, USA

Received 18 November 2009; received in revised form 9 March 2010; accepted 10 March 2010

Abstract

High spatial resolution measurements of interseismic deformation along major faults are critical for understanding the earthquake cycle and for assessing earthquake hazard. We propose a new remove/filter/restore technique to optimally combine GPS and InSAR data to measure interseismic crustal deformation, considering the spacing of GPS stations in California and the characteristics of interseismic signal and noise using InSAR. To constrain the longer wavelengths (>40 km) we use GPS measurements, combined with a dislocation model, and for the shorter wavelength information we rely on InSAR measurements. Expanding the standard techniques, which use a planar ramp to remove long wavelength error, we use a Gaussian filter technique. Our method has the advantage of increasing the signal-to-noise ratio, controlling the variance of atmosphere error, and being isotropic. Our theoretical analysis indicates this technique can improve the signal-to-noise ratio by up to 20%. We test this method along three segments of the San Andreas Fault (Southern section near Salton Sea, Creeping section near Parkfield and Mojave/Big Bend section near Los Angeles), and find improvements of 26%, 11% and 8% in these areas, respectively. Our data shows a zone of uplift to the west of the Creeping section of the San Andreas Fault and an area of subsidence near the city of Lancaster. This work suggests that after only 5 years of data collection, ALOS interferograms will provide a major improvement in measuring details of interseismic deformation.

Keywords: GPS; InSAR; Crustal deformation; PBO; Interseismic deformation; ALOS; ERS

1. Introduction

Recent studies (Smith-Konter and Sandwell, 2009) propose that near-fault strain rate (an indirect measure of stress rate) is inversely proportional to the earthquake recurrence interval, thus it is important to measure the variations in strain rate along all active faults. Strain rate is the spatial derivative of the velocity field (Jin and Park, 2006; Payne et al., 2008); so to be useful, geodetic measurements must have both high precision (~1 mm/yr) and high spatial resolution (~0.5 km) (Smith-Konter et al., 2008). In addition, strain rate maps must span the full length of a fault system (~2000 km). A comparison of strain rate maps of the San Andreas Fault (SAF), produced by 10 different research groups, using basically the same GPS velocity measurements, reveals that modeled strain rate can differ by factors of 5–8 times, with the largest differences occurring along the most active parts of the SAF (Sandwell et al., 2009). These large differences in estimated strain rate are not related to errors in vector GPS measurements but are due to the differences in methods used to construct a high resolution model using sparse GPS data sampling (~10 km). To achieve a 0.5-km spatial sampling of deformation measurements requires either a dramatic densification of the GPS velocity measurements, which is costly and therefore unlikely to take place, or the use of a higher resolution technique, such as interferometric synthetic aperture radar (InSAR).

GPS and InSAR are highly complementary methods for measuring surface deformation. GPS data provides high

* Corresponding author. Tel.: +1 858 822 4347.
E-mail address: mwei@ucsd.edu (M. Wei).

0273-1177/$36.00 © 2010 COSPAR. Published by Elsevier Ltd. All rights reserved.
doi:10.1016/j.asr.2010.03.013

precision (mm/yr) vector displacements at high temporal sampling rates and a moderate spatial sampling (~10 km). Because of its high precision and availability in our study region along the San Andreas Fault, GPS data have been used to study large-scale interseismic surface deformation, as well as to improve our understanding of fault zone deformation process (Feigl et al., 1993; Bennett et al., 1996; Segall and Davis, 1997; Smith and Sandwell, 2003; Meade and Hager, 2005; Jin et al., 2007; Wdowinski et al., 2007). The main weakness of using only GPS array data is that the spacing of, for example, the continuous GPS stations (CGPS) of the EarthScope Plate Boundary Observatory (PBO) project, is not adequate for resolving high velocity gradients (i.e., areas of high strain rate) which usually occur near active faults. Alternatively, InSAR data has sub-cm precision, a moderate temporal sampling rate (~10–50 days) and a high spatial sampling (~100 m), so theoretically it could provide the short spatial scale information currently lacking in CGPS data.

There have been many investigations that combine GPS and InSAR to optimally measure coseismic deformation (Massonnet et al., 1993, 1994; Peltzer et al., 1994; Zebker et al., 1994; Sandwell et al., 2000; Agnew et al., 2002; Jonsson et al., 2002; Simons et al., 2002; Fialko, 2004b; Johanson et al., 2006; Tong et al., 2010), post-seismic deformation (Massonnet et al., 1994, 1996; Peltzer et al., 1996; Pollitz et al., 2001; Fialko, 2004a; Johanson et al., 2006), interseismic deformation (Fialko, 2006), landslides (Rotta and Naglerb, 2006), seismic damage in urban area (Sugaa et al., 2001), and volcano deformation (Tomiyama et al., 2004; Sandwell et al., 2008). Methods for processing and stacking the InSAR data are described in many previous studies (Goldstein and Werner, 1998; Massonnet and Feigl, 1998; Sandwell and Price, 1998; Burgmann et al., 2000; Rosen et al., 2000; Ferretti et al., 2001; Hanssen, 2001).

The standard method for combining GPS and InSAR data involves removal of a reference model from each interferogram (usually based on GPS). Then a planar ramp is removed to minimize the orbit and other long wavelength errors. Next, the residual phase of the interferograms is averaged (stacking). Finally, the reference model is added back to the normalized stack.

This paper is a minor variant on this basic approach where we use a high-pass filter rather than removing a ramp to reduce the long wavelength errors in the InSAR data (Fig. 1). We call this process remove/filter/restore. There are several advantages of our technique. First, the filter not only removes the long wavelength error, but also reduces the intermediate wavelength atmospheric error. Second, the filtering method gives us more control over the variance of atmospheric noise. Moreover, the filtering has the benefit of being isotropic. It is independent of the number of frames used in the analysis, whereas in the ramp method the length scale of the polynomial depends on the size and shape of the area.

2. Technique design and theoretic performance

We develop and test our proposed technique, with a focus on measuring interseismic deformation along the SAF. First, we determine the optimal wavelength of the filter by analyzing the characteristic spacing of the GPS stations. Second, we estimate the effect of filtering on both atmospheric noise and interseismic signal, to bracket the effects of signal-to-noise ratio. Finally, in order to test if our method is an improvement over the standard techniques, we use both methods to combine GPS and InSAR data and compare the results in three areas: the Salton Sea area in Southern California, Parkfield in Central California and the Mojave/Big Bend section of the SAF in Southern California. Our overall objective is to determine how high-pass filtering of the InSAR data improves the signal-to-noise ratio and to estimate how many interferograms are required for a signal-to-noise ratio to exceed 1 along a particular fault segment.

2.1. Optimal wavelength

Our first step is to determine the minimum deformation wavelength that can be resolved by GPS stations in California. Using a nearest-neighbor analysis of the distance between the GPS stations (Fig. 2b), we find mean and median distances of 8.8 and 6.5 km, respectively. In addition, we calculate the distance from all of the GPS stations to the nearest location on the SAF and compile histograms of the spatial distribution of the GPS stations (Fig. 2c and d). We normalize the cumulative histogram to find the characteristic distance from GPS stations to the primary SAF (Fig. 2c and d). We use a 5-km bin size for the histograms and subdivide the SAF into ~200 segments along its entire 1000 km length. Thus, we divide the num-

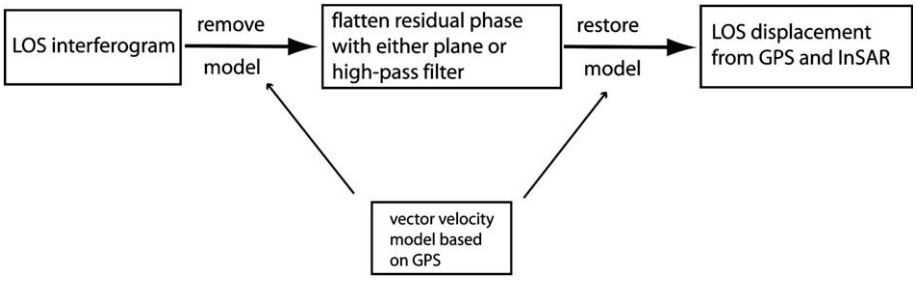

Fig. 1. Flow chart for combining InSAR and GPS using the remove/filter/restore method.

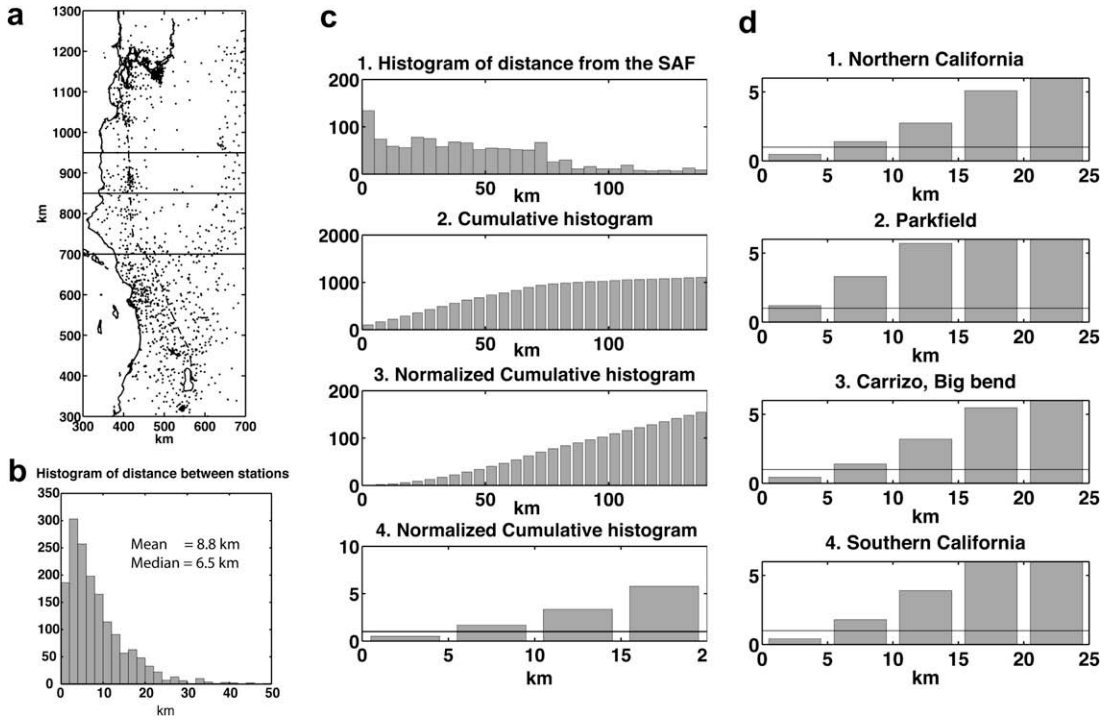

Fig. 2. GPS spacing in California, including EarthScope PBO and campaign GPS. (a) GPS distribution in California and the San Andreas Fault projected into pole of rotation (PoR) coordinates (Wdowinski et al., 2007). The dashed line is the main trace of the SAF and the dots are GPS stations used in this study. (b) Histogram of relative distance between GPS stations. The bin size is 5 km. (c1) Histogram of distance from GPS stations to the SAF with 5 km bins. The cumulative histogram (c2) is normalized in a way that divides the number of stations within a given distance from the fault by the number of segments (200) the SAF (c3 and c4 (zoomed view)). (d) Normalized cumulative histograms for four groups: (d1) Northern California (marked in (a) with y-axis ranging from 950 to 1300 km); (d2) Central California near Parkfield (850–950 km); (d3) Carrizo and Big Bend (700–850 km); (d4) Southern California (400–700 km). On average, the distance of one GPS station to the SAF, available in area d2, is 0–5 km and other three areas are 5–10 km.

ber of GPS stations within a 5-km region by 200 and get the average number of GPS stations within 5 km segments. Based on these analyses, the characteristic spacing of GPS stations in California is 5–10 km. We ask, given this characteristic spacing of the current GPS array what is the minimum spatial wavelength we can measure? Assuming a uniform spacing, the minimum resolvable wavelength is twice of the sample spacing. With non-uniform spacing, which is a more accurate representation of the GPS stations in California, the minimum resolvable wavelength should be 3–4 times of the mean sample spacing. Therefore, the average minimum wavelength of the signal that the GPS array can resolve is about 15–40 km. We chose the higher end, 40 km, as the wavelength of the filter we use in the following sections in this study.

2.2. Effect of filtering on noise

The main sources of noise for InSAR measurements are orbital, atmospheric, ionospheric, topographic, unwrapping and decorrelation errors (Hanssen, 2001). Ionosphere errors in California and orbital errors are typically global in scale ($> \sim$100 km), so they produce a ramp across a single 100 km $\times$ 100 km interferogram and the ramp is commonly removed/adjusted to the far-field velocity from GPS or tectonic models. The dominant error at scales less than or equal to the swath width of an interferogram ($< \sim$100 km) is the atmospheric delay, which is mostly related to spatial variations in atmospheric water vapor. Previous researchers have used various techniques to estimate or reduce the errors from the atmospheric delay, including statistical analysis (Goldstein, 1995; Emardson et al., 2003; Lohman and Simons, 2005), stacking indepen-

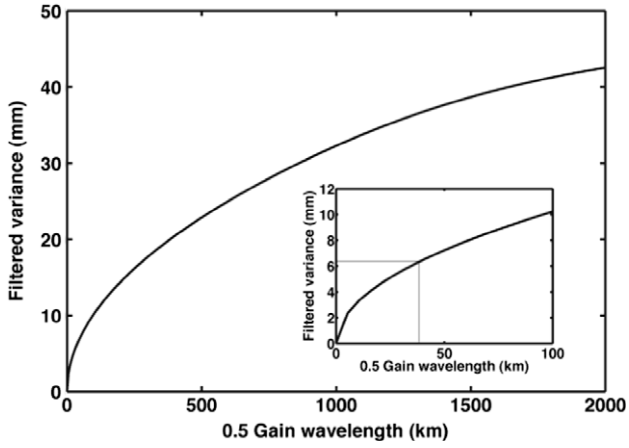

Fig. 3. The variance of the filtered atmospheric noise for filters with different wavelength. The inset figure is a zoomed in view at 0–100 km along the x-axis, where the grey box indicates the 40 km wavelength variance cutoff.

Please cite this article in press as: Wei, M., et al. Optimal combination of InSAR and GPS for measuring interseismic crustal deformation. J. Adv. Space Res. (2010), doi:10.1016/j.asr.2010.03.013

dent data (Schmidt et al., 2005), applying a weighted power spectral density filter (Ferretti et al., 2000; Schmidt and Burgmann, 2003), and correction using empirical methods (Elliott et al., 2008) or models derived from external data (Li et al., 2006; Doin et al., 2009). The limitation of using atmospheric delay models is that their resolution is usually too coarse. For example, the resolution is 1.125° for ERA40 (Uppala et al., 2005) and 32 km for the North American Regional Reanalysis (Mesinger et al., 2006). Here, we propose to use a Gaussian filter to reduce the atmospheric noise in InSAR data.

We determine the effect of spatial filtering on the atmospheric noise based on published noise models (Hanssen, 2001; Emardson et al., 2003) and mathematic derivations. A detailed process of this method is described in Appendix A and the result is shown in Fig. 3. Although the variance of atmospheric noise varies between different interferograms, based on GPS data Emardson et al. (2003) found a typical value of 2500 mm^2. The variance of the filtered atmospheric noise decreases after being high-pass filtered. Based on our calculation, the variance decreases from 100 mm^2 with a Gaussian filter with a 0.5 gain wavelength of 100 km to 36 mm^2 with a Gaussian filter of 40 km. Later, we use this noise model to estimate how signal-to-noise ratio change with filter wavelength.

2.3. Effect of filtering on interseismic signal

The interseismic signal of the SAF can be estimated from dislocation models partly constrained by GPS data

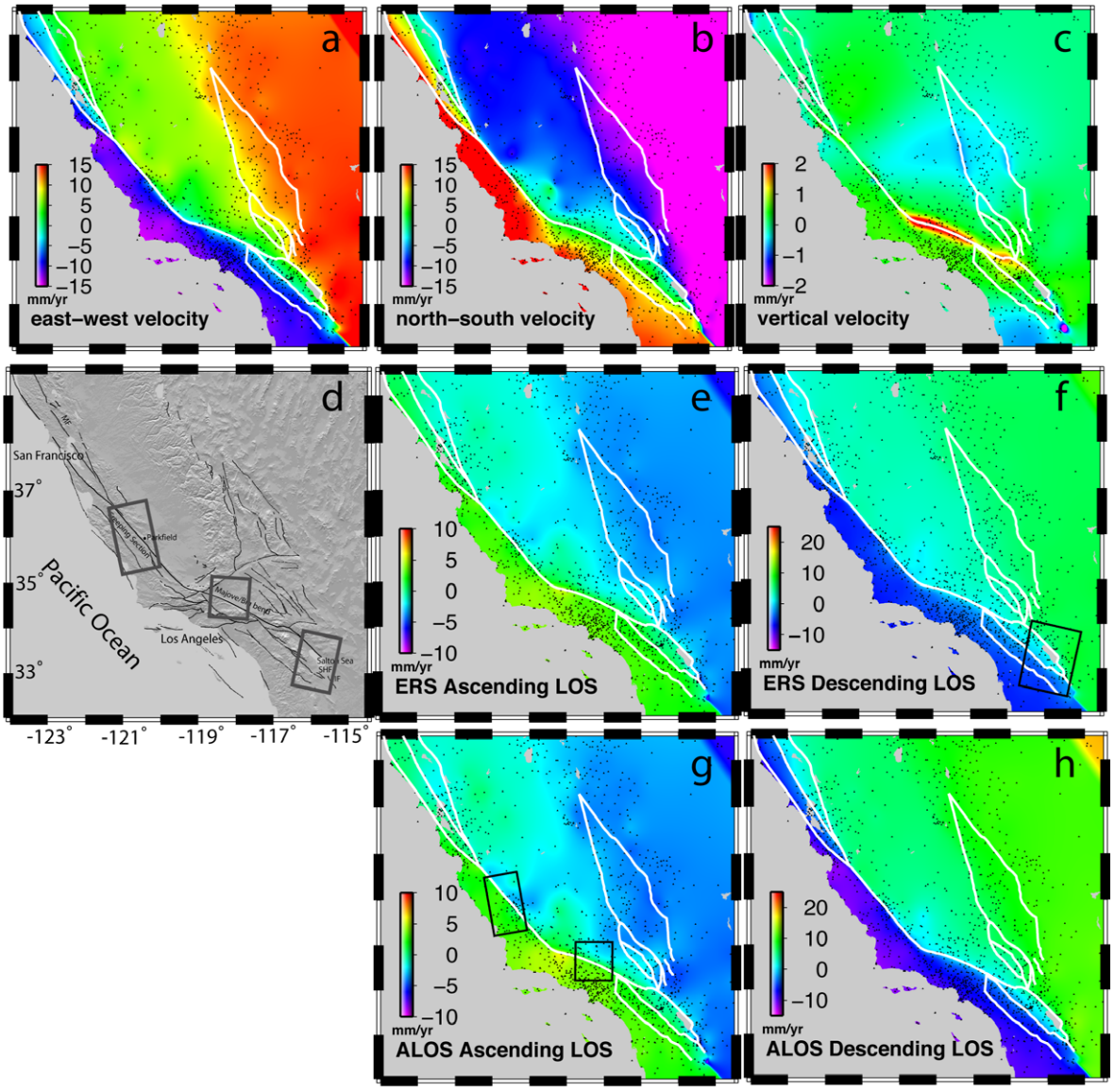

Fig. 4. (a–c) East, north and vertical velocities from combined dislocation model and spline fit. White soild lines represent the major faults. (d) Topography shaded map of the research area. Grey boxes show the locations of InSAR data used in this study. Fault names are abbreviated as follows: MF, Maacama fault; SHF, Superstition Hills fault; IF, Imperial fault. (e and f) Line-of-sight velocity for ascending and descending passes of ERS interferometry at 23° look angle and (g and h) ALOS interferometry at a 34.3° look angle. Modeled faults are shown in white. Black triangles are the GPS stations. Black boxes in ERS descending and ALOS ascending are the InSAR used in this study, same as grey boxes in (d).

Please cite this article in press as: Wei, M., et al. Optimal combination of InSAR and GPS for measuring interseismic crustal deformation. J. Adv. Space Res. (2010), doi:10.1016/j.asr.2010.03.013

(Fig. 4; Appendix B). Our models suggest the horizontal velocity components have 40 km and larger scale variations in associated with a spline fit superimposed on the large-scale pattern generated by dislocation motion at depth. Our vertical velocity models only include the large-scale dislocation pattern, and show mostly small velocities except along the compressional bends of the SAF north of Los Angeles, as well as the small extensional bends south of the Salton Sea and in the Cierro Prieto geothermal area, where subsidence can exceed 3 mm/yr. We believe that our dislocation model, or any dislocation model having variations in locking depth, provides a reasonable estimate of the spatial variations in the true velocity field. To determine the expected base model for InSAR data, the 3D velocity model is projected into the InSAR line-of-sight (LOS) direction for both ERS and ALOS, most commonly used InSAR satellite so far (Fig. 4). Our results show that because of the fault geometry, descending tracks are more sensitive to fault. High-pass filtering of the LOS models at 40 km wavelength reveals a signal that is outside the band recoverable by GPS point measurements (Fig. 5b2). Our high-pass filtered velocity has the largest variations near the SAF. The amplitude of the filtered LOS velocity decreases as the wavelength of the high-pass filter is decreased. The 40 km optimal wavelength, as determined from the characteristic spacing of GPS stations in California, results in high-pass filtered residual rates of <5 mm/yr. Based on this analysis, the stacked interferograms need to have a precision better than 5 mm/yr in order to provide new information on the interseismic velocity field.

2.4. Effect of filtering on signal-to-noise ratio

Our next step is to estimate how filtering affects the signal-to-noise ratio of InSAR data measuring the interseismic deformation. In general, filtering will tend to decrease the amplitude for both signal and noise, but can increase the signal-to-noise ratio (Fig. 5c). We use the dislocation model described in Appendix B as the expected signal and the noise model described in Appendix A as the expected noise. The amplitude and wavelength of the signal is different along different faults in California. We selected four regions to quantify the effect of the filtering on signal-to-noise ratio: the Maccaama fault in Northern California, the Creeping section of the SAF in Central California, the Mojave/Big Bend in Southern California and the Imperial fault in Southern California (Fig. 5c). The maximum positive signal with these four areas is plotted versus the wavelength of the filter. We find that in all four areas the signal-to-noise ratio increases as the wavelength decreases, however the change in the signal-to-noise ratio is greatest along Creeping section because of the step-like signal due to fault creep, showing an increase of 20% using a 40-km wavelength filter. The importance of the SNR curve (Fig. 5c) is the trend but not the absolute value. The SNR is computed from a single interferogram with a

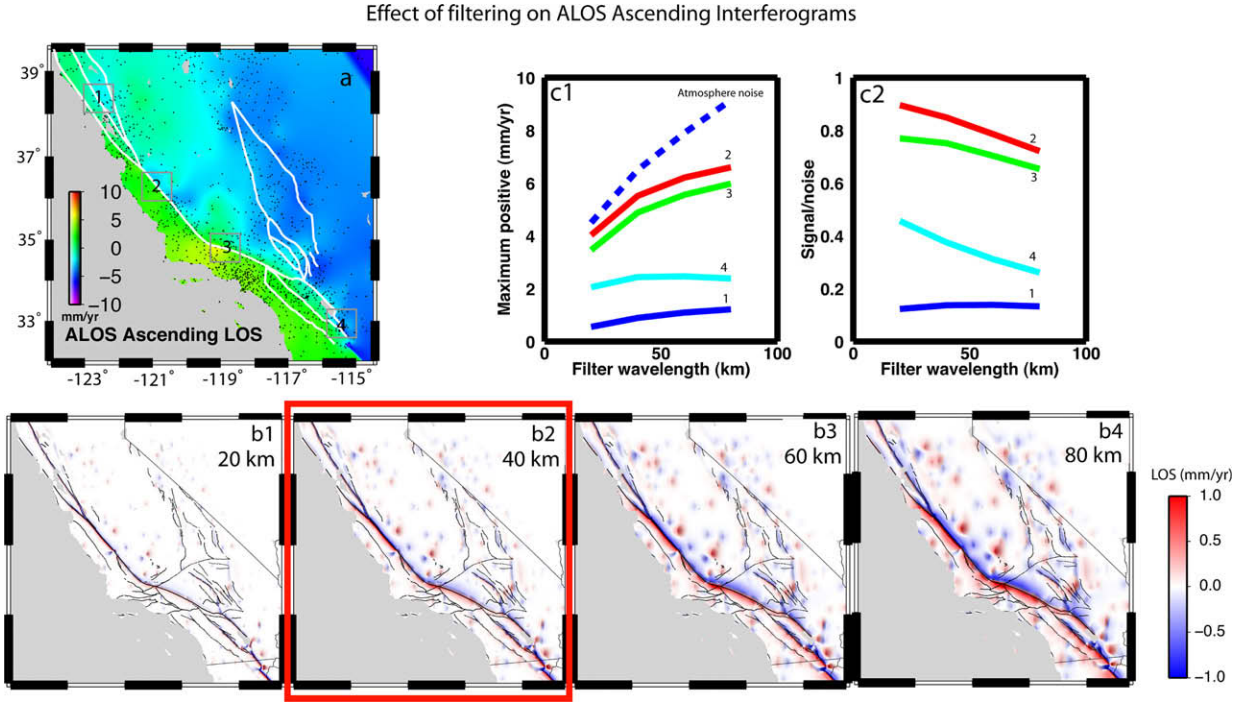

Fig. 5. Filter effect on interseismic signal observed by ALOS ascending interferograms. (a) A synthetic ALOS ascending interferogram based on a deformation model constrained by GPS data. A constant look angle (34.5°) is used here. (b1–4) Filtered interferograms with different Gaussian filters. The number on the top right corner (20, 40, 60, 80 km) is the 0.5 gain wavelength of the Gaussian filter. (c1–2) Relationship of how the four different areas (1–4, see Fig. 3a) respond to different filter wavelengths. (c1) Maximum signal as a function of filter wavelength. (c2) Signal-to-noise ratio as a function of filter wavelength. As the data shows, filtering can increase the signal-to-noise ratio by as much as 20% compared to no filtering.

Please cite this article in press as: Wei, M., et al. Optimal combination of InSAR and GPS for measuring interseismic crustal deformation. J. Adv. Space Res. (2010), doi:10.1016/j.asr.2010.03.013

1-year interval, and therefore the SNR value is typically less than 1. However, we can increase the SNR by stacking multiple interferograms from more than 1-year intervals.

2.5. Test the new technique in three areas

We next test this method with real data, by processing 14 ERS-1/2 descending interferograms near the Salton Sea spanning 1992–2008 (Fig. 6a), 6 ALOS ascending interferograms near the Creeping section of SAF spanning 2006–2009 (Fig. 6b), and 12 ALOS ascending interferograms near the Mojave/Big Bend section of the SAF spanning 2006–2009 (Fig. 6c). We selected these three areas because of the observed active faults and crustal motion, thus providing an adequate setting for testing our technique. ERS data covers more than 10 years near the Salton Sea and is provided by the European Space Agency through the WINSAR archive. For the ERS data at the Salton Sea area, we processed two frames, 2925 and 2943, to better estimate the long wavelength error. There are 14 ERS descending interferograms with average time intervals of 3–5 years available. ALOS data are provided by JAXA and obtained through the Alaska Satellite Facility, as well as the ALOS User Interface Gateway (AUIG). Since ALOS only has limited acquisition in California and the baseline has been drifting by more than 6 km following the launch in February 2006 through early 2008, we only identified 6 interferograms near the Creeping section of SAF suitable for this study, but 12 interferograms were available in the Mojave/Big Bend fault region. One of the major advantages of using the longer wavelength L-band data with respect to the C-band data is that for small deformations, a plane can be removed from the residual interferograms to remove any possible phase wrap. Therefore phase unwrapping is not needed, allowing the entire area of interferogram be used in the stack. The InSAR data was processed using SIOSAR software (Wei et al., 2009), and SRTM data were used to remove the effects of topography.

We processed these data with two methods: filtering the residual and removing a ramp. A Gaussian filter with a half gain at 40 km was used in the first method. For the removing a ramp method, both quadratic (Wright et al., 2004) and linear plane (Gourmelen et al., 2007) have been used, depending on how many frames were processed. Here, we used a 6-parameter quadratic plane to fit the ramp.

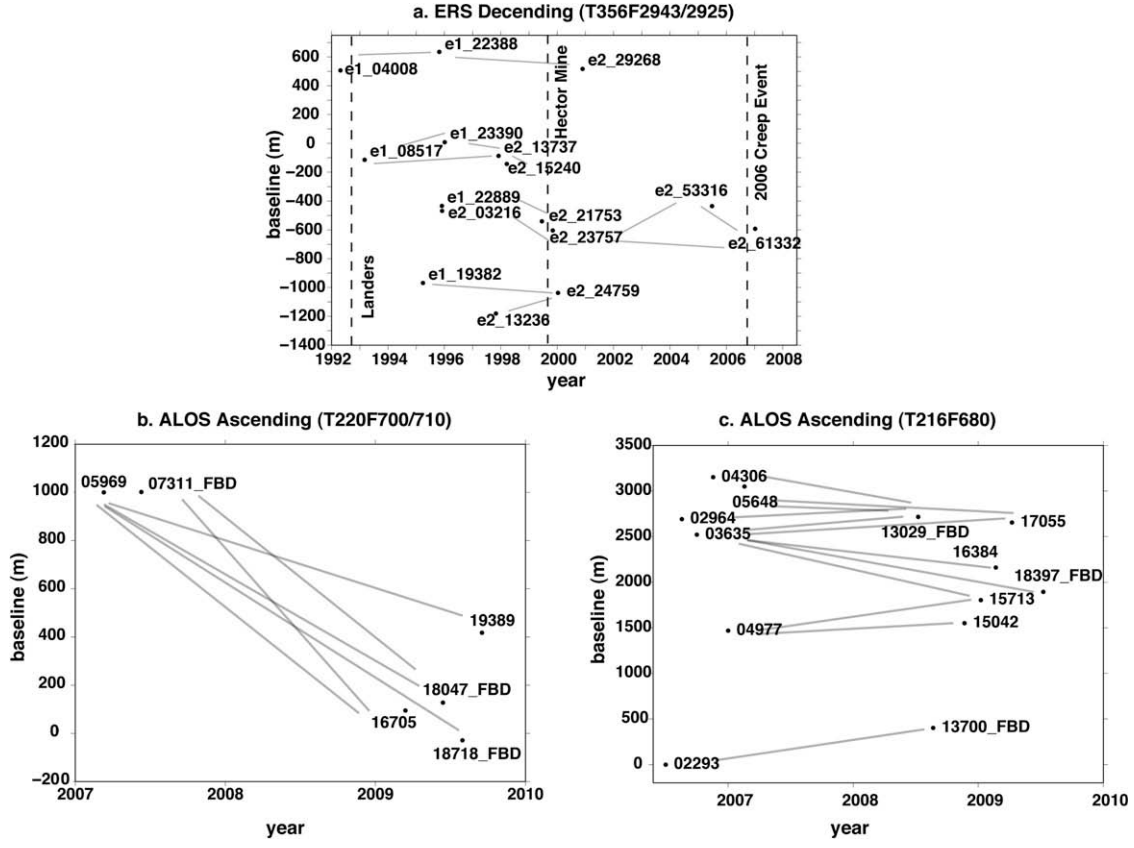

Fig. 6. InSAR data used in this study for the Salton Sea region in Southern California, the Creeping section of the SAF in Central California and the Majave/Big Bend fault region in Southern California. (a) ERS descending data (Track 356 Frame 2943/2925). The dashed lines label the times of the Landers and Hector Mine earthquakes, and the 2006 creep event on the Superstition Hills fault. Fourteen ERS descending interferograms with average time intervals of 3–5 years are available for use. (b) ALOS ascending data (Track 220 Frame 700/710) along the Creeping section of the SAF. Six ALOS ascending interferograms with average time intervals about 1.5–2 years are available for use. (c) ALOS ascending data (Track 216 Frame 680) in the Majave/Big Bend fault region. Twelve interferograms with average time interval of 2 years are available for use.

Please cite this article in press as: Wei, M., et al. Optimal combination of InSAR and GPS for measuring interseismic crustal deformation. J. Adv. Space Res. (2010), doi:10.1016/j.asr.2010.03.013

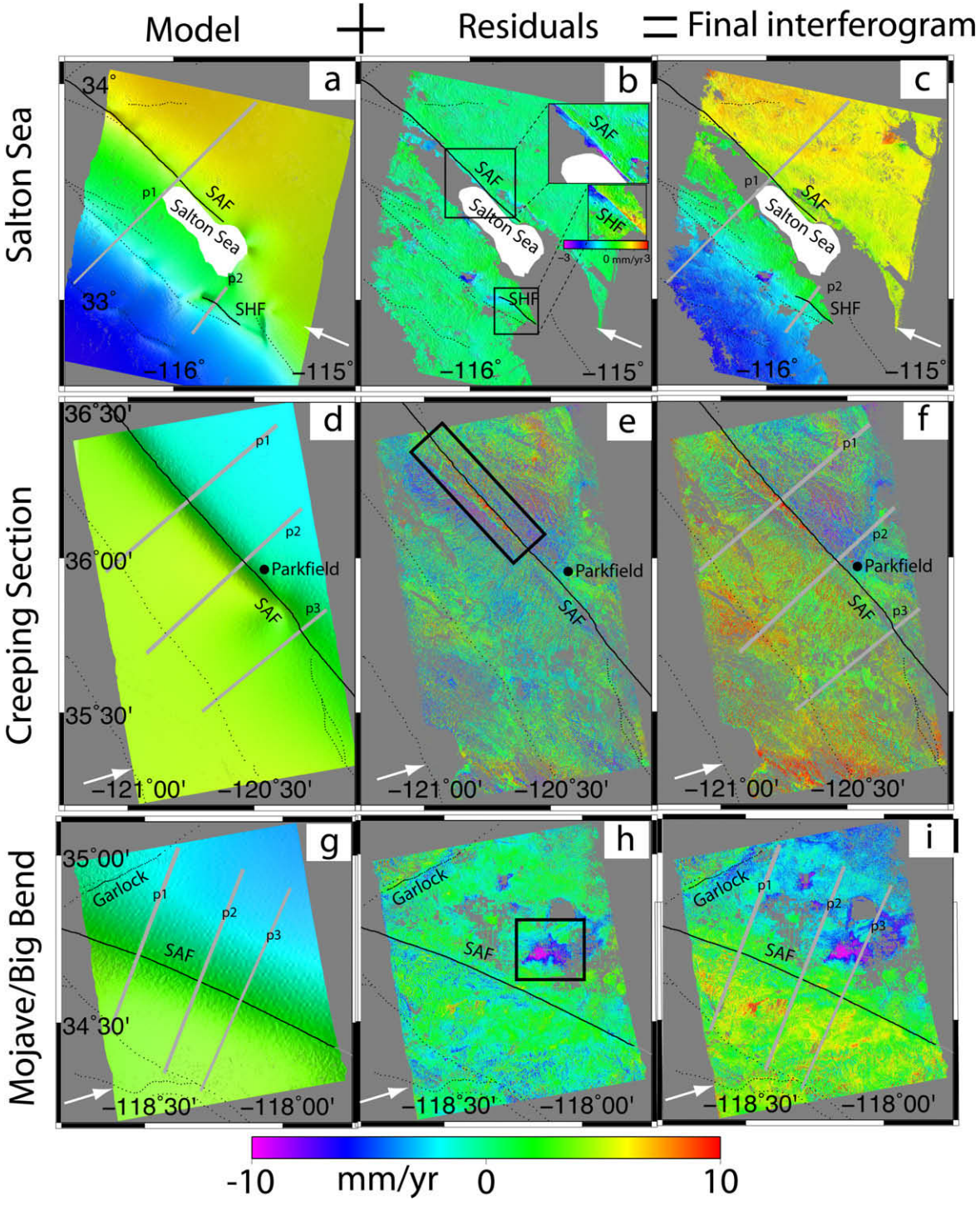

Fig. 7. Interferograms using the filtering method in the three areas: the Salton Sea, the Creeping section of the SAF and the Mojave/Big Bend fault region. (a, d and g) Base model constrained by the GPS data. (b, e and h) Stacked residual interferograms after applying the filtering method. (c, f and i) The final interferogram is the sum of base model and the residual interferogram. Black solid line shows the main fault trace of the San Andreas Fault and Superstition Hills Fault. Black dots show the other secondary faults. Grey solid lines show the locations of the profiles in Fig. 8. White arrow indicates the satellite look direction. Black boxes in (b, e and h) highlight the area with short wavelength signals. Two insets in (b) show creep of the SAF and the SHF, with a different color scale.

The InSAR contribution to the measurement of a short wavelength signal is shown for three focus areas (Fig. 7). Far from the fault, the velocity largely matches the GPS-based model whereas the interferograms sometimes provide new details near the fault (for example, fault slip near the Superstition Hills fault in Fig. 7b, fault creep and local uplift in Fig. 7e, and local subsidence due to ground water extraction in Fig. 7b and h). Another way to show the con-

Please cite this article in press as: Wei, M., et al. Optimal combination of InSAR and GPS for measuring interseismic crustal deformation. J. Adv. Space Res. (2010), doi:10.1016/j.asr.2010.03.013

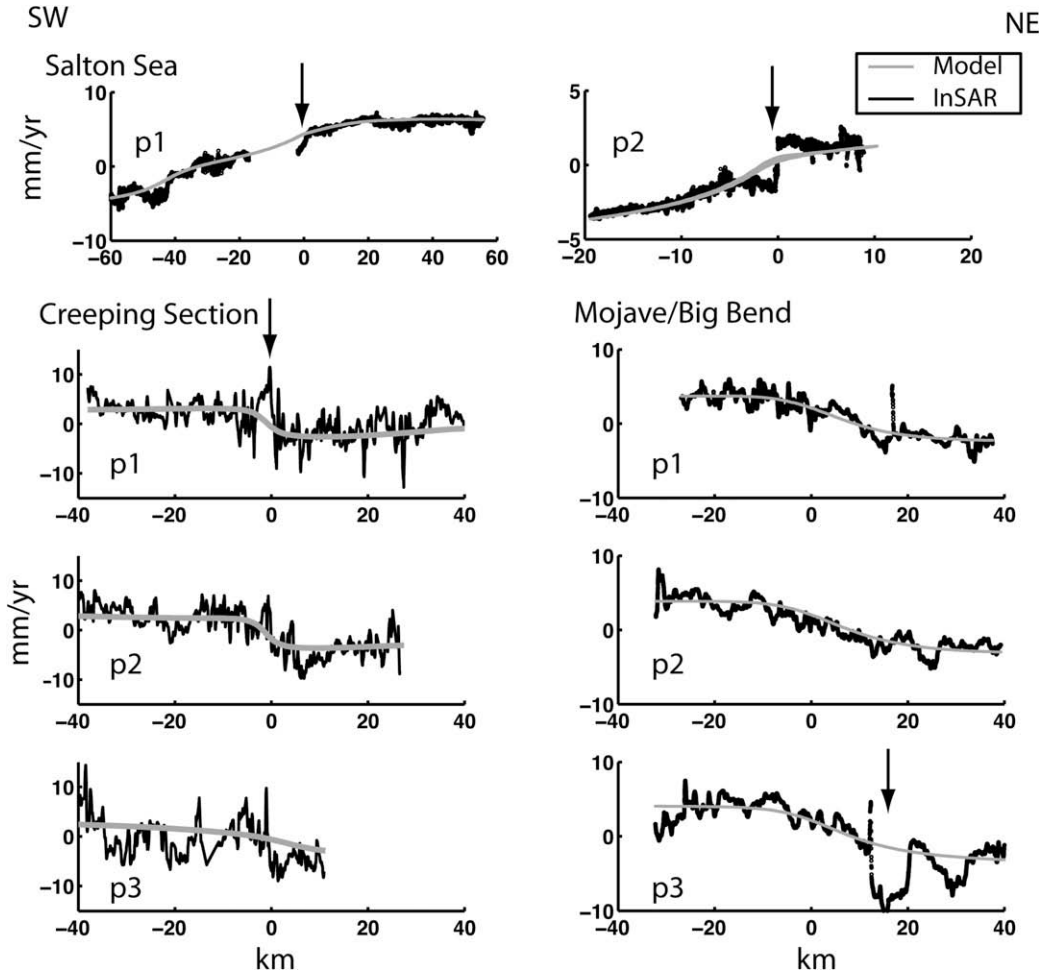

Fig. 8. Profiles across main faults in three study areas. Arrows identify short wavelength signals that are absent in GPS data. All InSAR data is one-dimensional low pass filtered with a Gaussian filter of 500 m wavelength. This 1D filter is different from the filter we used as the filter versus ramp treatment of the data.

tribution of InSAR is to look at the profiles of the interferograms in our three study areas (Fig. 8). The profile across the Superstition Hills Fault (SHF) in the Salton Trough is about 1 km wide (fault parallel direction) and 30 km long, whereas other profiles are ~1 km wide and 80 km long. For illustrative purposes, to compare the InSAR data of the Creeping and Mojave/Big Bend areas (which are rather noisy) with base model profiles, the InSAR data profiles are robustly filtered with a Gaussian filter with 500 m (i.e., where we replace outliers with a median value during filtering). The profiles for the Salton Sea region have very high signal-to-noise ratio and this additional filtering step is not necessary. In the Salton Sea area, as the profiles show, step-like signal near the SAF and the SHF exist, which have been previously studied (Lyons and Sandwell, 2003; Fialko, 2006; Wei et al., 2009). In the Creeping section of the SAF, a possible uplift with amplitude of about 1 cm/yr is observed, although it could be an anomaly caused by two strands of the fault trace. In the Mojave/Big Bend area, we find subsidence of 1 cm/yr, which is probably due to ground water extraction (Peltzer et al., 2001). As shown in Figs. 7 and 8, InSAR can reveal short wavelength signals that GPS data miss.

We compare the results of residual filtering and ramp removal using ERS and ALOS data, as well as the GPS data (Fig. 9 and Table 1). For the GPS data comparison, only PBO sites are used because they have both horizontal and vertical measurements. Three components of the PBO GPS measurements are projected into the LOS. In the Salton Sea area (Fig. 9c), the difference between the ramp and filter method is mainly caused by long wavelength coseismic deformation from the 1992 Landers and 1999 Hector Mine earthquakes, both of which are not accurately included in our base model. For the Creeping section (Fig. 9f), the difference between the two methods is a round shape anomaly with a diameter of 50 km and amplitude of 3–4 mm/yr. Significant differences between the GPS and interferogram velocities are mainly located in the lower part of the image, with a maximum of 10 mm/yr. However, the difference in the filtered interferogram is smaller for several stations in the middle of the image. For the data near the Mojave/Big Bend fault region (Fig. 9i), two areas of

Please cite this article in press as: Wei, M., et al. Optimal combination of InSAR and GPS for measuring interseismic crustal deformation. J. Adv. Space Res. (2010), doi:10.1016/j.asr.2010.03.013

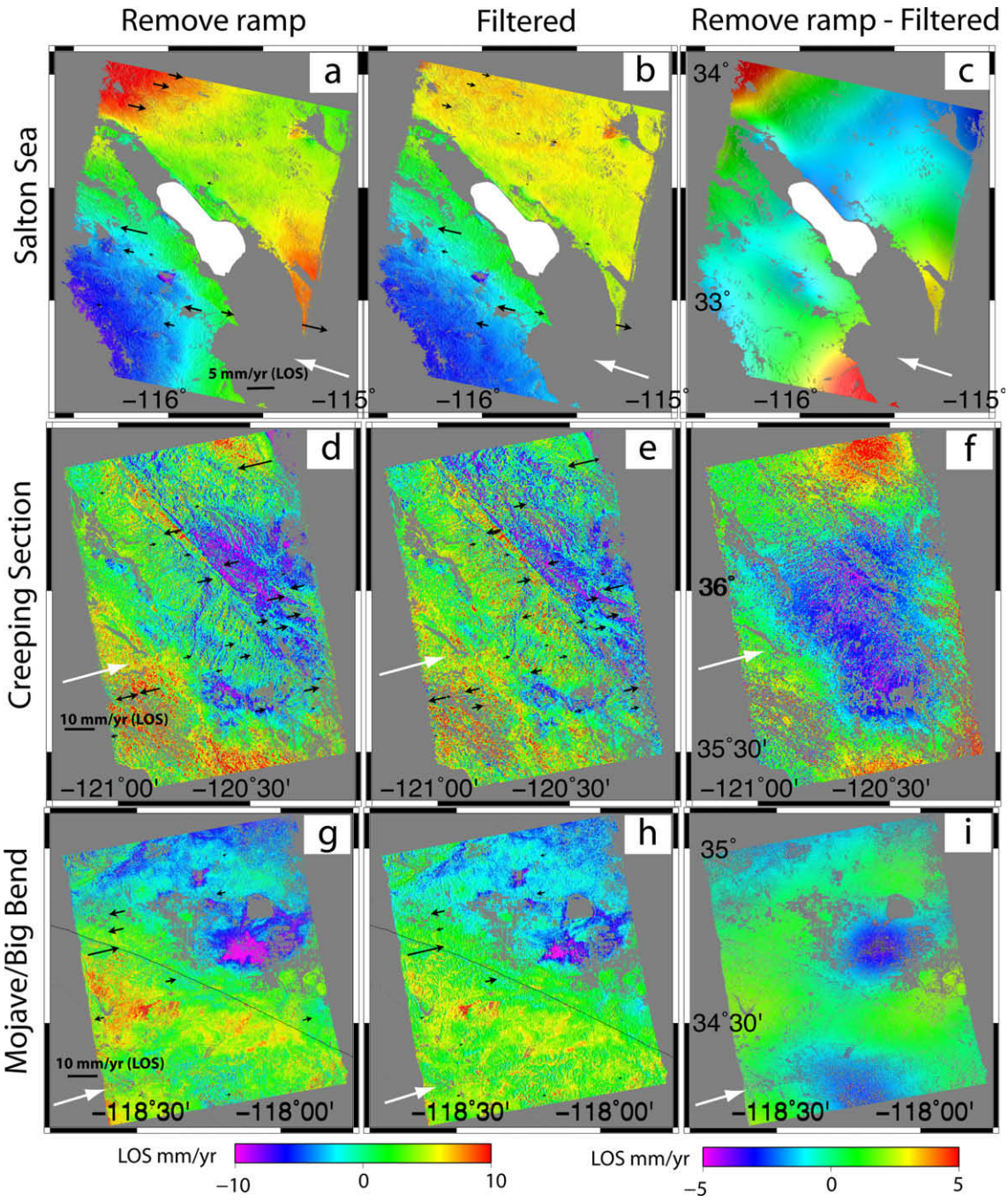

Fig. 9. Interferograms for two different methods in the three areas: the Salton Sea, the Creeping section of the SAF and the Mojave/Big Bend fault region. (a, d and g) Ramp removal, (b, e and f) filter and (c, f and i) their difference. Black arrows are the difference between GPS measurements (projected to LOS) and the interferograms. The arrows pointing toward the east represent a negative interferogram − GPS difference, or that the interferogram deformation is less than the GPS. Arrows pointing west reflect the opposite case. The white arrow indicates the satellite look direction. In (c, f and i), positive values indicate that the ramp-removed interferogram is larger (in a positive sense) than the filtered interferogram in the LOS direction.

high difference with a magnitude of 2–3 mm/yr exist. The feature in the middle of the image is mainly caused by the effect of filtering a subsidence signal in the Mojave/Big Bend fault region due to ground water extraction, while the feature in the lower part of the image is unknown. Improvement is much easier to detect in the lower part of the image. This is caused by the different processing methods, where the large difference is due to the atmospheric error, as well as coseismic deformation from the Landers and Hector Mine earthquakes (Emardson et al., 2003; Lohman and Simons, 2005; Massonnet et al., 1993; Simons et al., 2002; Zebker and Rosen, 1997; Zebker et al., 1994).

To evaluate the benefit of using a high-pass filter rather than a planar ramp, we calculated the standard deviation between the final model (filter and ramp) and the GPS data projected into the radar line-of-sight. Although the filter

Please cite this article in press as: Wei, M., et al. Optimal combination of InSAR and GPS for measuring interseismic crustal deformation. J. Adv. Space Res. (2010), doi:10.1016/j.asr.2010.03.013

Table 1
Misfit between base model, filtered InSAR, ramp removed InSAR and PBO GPS stations. Three components of GPS velocity are projected to the satellite line-of-sight direction.

	Number of interferograms	Number of PBO GPS stations	Misfit to GPS (LOS mm/yr)			
			Base model	InSAR filter	InSAR ramp	Improvement (filter versus ramp) (%)
Salton Sea	14	18	2.5	2.6	3.5	26
Creeping section	6	35	2.7	3.4	3.8	11
Mojave/Big Bend	12	13	3.7	4.0	4.3	8

method produced a smaller misfit, the difference is not statistically significant (Table 1). The greatest difference is in the Salton Sea area (18 GPS, 2.6 mm/yr filter, 3.5 mm/yr ramp), which is mostly due to fact that the ramp method cannot effectively remove the coseismic deformation of the Landers and Hector Mine earthquakes in this dataset. A coseismic model is required to improve the misfit if one wants to use the ramp method. Based on this analysis, it is not conclusive which technique is better or more accurate. However, the filtering method gives us more control over the variance of atmospheric noise. Also the filtering is independent of the number of frames used in the analysis, while the ramp depends on the size and shape of the area. In other words, the ramp will not be isotropic if the area is not square, but filtering will always be isotropic.

Note that these standard deviations of both filtering and ramp method are larger than the misfit between the model and GPS data. This is expected because the combined solution has many more degrees of freedom as represented by shorter wavelengths. We expect that the combined solution will provide a more accurate representation of the strain field than using GPS alone.

3. Discussion

The spatial covariance parameter σ_e in the model we adopted from Emardson et al. (2003) has variability, which is reflected as different atmospheric noise level in interferograms. The range of the variability is not provided in Emardson et al. (2003). As shown in Eq. (A17), the variability of σ_e will affect the number of interferograms required to resolve small interseismic signals. However, it will not affect the advantage of the filtering technique as long as the spatial characteristics of atmosphere are the same.

The technique we outline in this work can be used to improve our estimation and understanding of interseismic deformation, especially along the section of the SAF north of Los Angeles in the next few years. In the arid areas of Southern California, previous C-band InSAR satellites, ERS1/2 and ENVISAT, have acquired numerous datasets now that are available for analysis. However, temporal decorrelation due to vegetation has severely limited this type of analysis along the northern section of the SAF. The improved temporal decorrelation from the Japanese L-band satellite ALOS will allow us to apply InSAR in Northern California (Wei and Sandwell, 2010). However, the acquisition of ALOS in California is infrequent, at ~2–4 images per year. At the time of this manuscript preparation (March, 2010), the ALOS dataset is not large enough to provide better constraints on the interseismic deformation. Based on our present calculations of the deformation signal and noise of ALOS data, we estimate that 5-years of ALOS data will be needed to improve the interseismic models using InSAR. The greatest improvements will be in Northern California where GPS measurements are sparse. All processing and model codes utilized here are publicly available (http://topex.ucsd.edu).

4. Conclusions

We have developed a remove/filter/restore technique to combine GPS and InSAR data optimally. This technique is based on the analysis of the spacing of EarthScope PBO and campaign GPS, and the characteristics of the signal and noise in InSAR data. We estimate the improvements of signal-to-noise ratio in InSAR data for measuring interseismic deformation in California. Because the residual interseismic signal and noise have different scale dependencies, filtering an interferogram can increase the signal-to-noise ratio by as much as 20%. Applying this procedure to a large stack of ERS1/2 interferograms in the Salton Sea, Southern California and ALOS interferograms near Parkfield, Central California and Mojave Desert/Big Bend, Southern California, we find improvements in all three areas using the new technique. Our analysis shows that ALOS data will be able to make major contributions toward measuring interseismic deformation after collecting data for 5 years in orbit.

Appendix A. The effect of high-pass filtering on atmospheric error

Assume the phase of the interferogram $p(\vec{x})$ has two parts:

$$p(\vec{x}) = s(\vec{x}) + n(\vec{x}) \tag{A1}$$

where $\vec{x}$ is two-dimensional spatial vector, $s(\vec{x})$ is the deformation signal and $n(\vec{x})$ is the atmospheric noise. Here we focus on the atmospheric noise, which is assumed stationary, random, and isotropic with zero mean.

Please cite this article in press as: Wei, M., et al. Optimal combination of InSAR and GPS for measuring interseismic crustal deformation. J. Adv. Space Res. (2010), doi:10.1016/j.asr.2010.03.013

The autocovariance of the noise is

$$C(\vec{x}) = \int\int n(\vec{x}_o)n(\vec{x}-\vec{x}_o)d^2\vec{x}_o \tag{A2}$$

where the integrals are performed over the area A of the interferogram.

By definition, the variance of the noise is

$$\delta^2 = C(0,0) = \int\int n^2(\vec{x})d^2\vec{x} \tag{A3}$$

and the standard deviation of the noise is

$$\sigma_{noise} = \sqrt{\delta^2/A} \tag{A4}$$

Now suppose that we filter the noise using an isotropic filter. What is the new filtered autocovariance function and variance? The filtered noise is

$$\hat{n}(\vec{x}) = \int\int f(|\vec{x}-\vec{x}_o|)n(\vec{x}_o)d^2\vec{x}_o \tag{A5}$$

where $f(|\vec{x}|)$ is a real-valued isotropic filter. Note that the Fourier transform of the autocovariance function is the power spectrum and is given by

$$C(\vec{k}) = N(\vec{k})N^*(\vec{k}) \tag{A6}$$

where $N(\vec{k}) = \int\int n(\vec{x})e^{-2\pi i(\vec{k}\cdot\vec{x})}d^2\vec{x}$.

Now we want to compute the autocovariance function and the variance of the filtered noise. The power spectrum of the filtered autocovariance is

$$\begin{aligned} C(\vec{k}) &= N(\vec{k})N^*(\vec{k}) = (N(\vec{k})F(|\vec{k}|))(N(\vec{k})F(|\vec{k}|))^* \\ &= F^2(|\vec{k}|)N(\vec{k})N^*(\vec{k}) \end{aligned} \tag{A7}$$

where $F(|\vec{k}|)$ is the Fourier transform of the filter which is real-valued and isotropic.

Using the convolution theorem, we can rewrite this as

$$C(\vec{x}) = \int_A\int g(|\vec{x}-\vec{x}_o|)C(\vec{x}_o)d^2\vec{x}_o \tag{A8}$$

where $g(|\vec{x}|) = \Im_2^{-1}(F^2(|\vec{k}|))$, and $\Im_2()$ and $\Im_2^{-1}()$ are the two-dimensional forward and inverse Fourier Transform. Then we assume that $C(\vec{x}_o)$ is an isotropic function, so the integration can be partly completed in cylindrical coordinates, where $d^2\vec{x} = rdrd\theta$. The integration becomes

$$C(r) = 2\pi\int_0^\infty g(|r-r_o|)C(r_o)r_o dr_o \tag{A9}$$

Next we use an autocovariance function of atmospheric noise based on signal delays in the GPS data from Southern California (Emardson et al., 2003). Their one-way noise variance model is

$$\sigma = cL^\alpha + kH \tag{A10}$$

where σ is the square root of variance in mm, L is the distance between two points in km and H is the height difference in km. c, α and k are constants with value of 2.5, 0.5 and 4.8, respectively, derived from the neutral atmospheric delays in GPS data in Southern California. This model is valid over a range of 10–800 km for L and 0–3 km for H. While α is basically site-independent, c depends on the location on the Earth.

If e_1 and e_2 are the observation errors corresponding to the observations d_1 and d_2, which are any two pixels within a given interferogram, the autocovariance between these two errors are

$$\begin{aligned} Cov(e_1,e_2) &= \frac{1}{2}Var(e_1) + \frac{1}{2}Var(e_1) - \frac{1}{2}Var(e_1-e_2) \\ &= \sigma_e^2 - \frac{1}{2}\sigma^2 \end{aligned} \tag{A11}$$

where σ_e^2 is defined as $Var(e) = \frac{1}{2}Var(e_1) + \frac{1}{2}Var(e_1)$. Based on the GPS data, Emardson et al. (2003) find σ_e is about 50 mm and σ is described as in Eq. (A10). Usually, the dependence of height difference can be dropped because it is much smaller than the distance dependence. Then the autocovariance function is

$$Cov(e_1,e_2) = \sigma_e^2 - \frac{c^2}{2}L^{2\alpha} \tag{A12}$$

Next, we use this function to calculate the covariance of the noise in a high-pass filtered interferogram. The Gaussian filter we use is

$$f(|\vec{x}|) = \frac{1}{2\pi\eta^2}e^{-\frac{|\vec{x}|^2}{2\eta^2}} = \frac{1}{2\pi\eta^2}e^{-\frac{x^2+y^2}{2\eta^2}} \tag{A13}$$

where η is the standard deviation of the Gaussian distribution and a characteristic wavelength. The Fourier transform of the Gaussian filter is

$$\begin{aligned} \Im_2[f(\vec{x})] &= \int\int \frac{1}{2\pi\eta^2}e^{-\frac{x^2+y^2}{2\eta^2}}e^{-2\pi i(\vec{k}\cdot\vec{x})}d^2\vec{x} \\ &= e^{-2\pi^2\eta^2(k_x^2+k_y^2)} \end{aligned} \tag{A14}$$

The inverse Fourier Transform of the squared Fourier Transform of the Gaussian filter is

$$\begin{aligned} \Im_2^{-1}[\Im_2^2[f(\vec{x})]] &= \int\int (e^{-2\pi^2\eta^2(k_x^2+k_y^2)})^2 e^{2\pi i(\vec{k}\cdot\vec{x})}d^2\vec{k} \\ &= \frac{1}{4\pi\eta^2}e^{\frac{x^2+y^2}{4\eta^2}} \end{aligned} \tag{A15}$$

We substitute Eqs. (A15) and (A12) into (A9). Then the filtered autovariance function is

$$\begin{aligned} C(r) = 2\pi\int_0^{L_{\max}} &\times \frac{1}{4\pi\eta^2}e^{-\frac{|r-r_o|^2}{4\eta^2}}\left(\sigma_e^2 - \frac{c^2}{2}(r-r_o)^{2\alpha}\right)r_o dr_o \end{aligned} \tag{A16}$$

where $L_{\max}$ is the maximum distance that Eq. (A10) is valid, which equals 800 km in Southern California (Emardson et al., 2003). We are most interested in the variance, which is Eq. (A16) at $r = 0$. Since $\alpha = 0.5$ based on GPS data, the integration is simplified to

Please cite this article in press as: Wei, M., et al. Optimal combination of InSAR and GPS for measuring interseismic crustal deformation. J. Adv. Space Res. (2010), doi:10.1016/j.asr.2010.03.013

$$C(0) = 2\pi \int_0^{L_{\max}} \frac{1}{4\pi\eta^2} e^{-\frac{r_o^2}{4\eta^2}} \left(\sigma_e^2 - \frac{c^2}{2} r_o\right) r_o dr_o$$
$$= \sigma_e^2 - \frac{c^2\eta\sqrt{\pi}}{2} erf\left(\frac{L_{\max}}{2\eta}\right) \quad \text{(A17)}$$

This is the result of the low-pass filter. To get the high-pass result, we need to subtract Eq. (A17) from the original variance,

$$\sigma_f^2 = \sigma_e^2 - C(0) = \frac{c^2\eta\sqrt{\pi}}{2} erf\left(\frac{L_{\max}}{2\eta}\right) \quad \text{(A18)}$$

We substitute parameters in Eq. (A17) with values, $\sigma_e = 50, L_{\max} = 800, c = 2.5$, then the standard deviation of the noise in the high-pass filtered data is

$$\sigma_f = \sqrt{3.125\eta\sqrt{\pi} erf\left(\frac{800}{2\eta}\right)}. \quad \text{(A19)}$$

Appendix B. Dislocation model

The vector velocity field cannot be completely resolved with point GPS measurements, so we use a dislocation model (1 km resolution), constrained by GPS velocities, to provide a complete vector field. We expect the model to be accurate at large scales especially away from the faults, but less accurate at smaller scales. We model the North American-Pacific plate boundary as a series of vertical connected fault dislocations imbedded in an elastic plate overlying a viscoelastic half-space (Smith and Sandwell, 2006). The dislocation model simulates interseismic strain accumulation, coseismic displacement and post-seismic viscous relaxation of the mantle. However, when considering the recent average EarthScope PBO velocity field (2004–2009), the interseismic part of the model dominates. Three types of data are used to estimate the parameters of the model: (1) long-term slip rates (i.e., over many earthquake cycles) are initially constrained by geologic estimates (Field, 2007) and then adjusted to ensure that the sum of the slip across the plate boundary is equal to the far-field estimate of 45 mm/yr. Slip rates are further adjusted to match contemporary geodetic estimates of far-field slip (e.g., Bennett et al., 1996; Freymeuller et al., 1999; Becker et al., 2005; Meade and Hager, 2005; Fay and Humphreys, 2005; Fialko, 2006). (2) Rupture history on each fault segment is based on historical accounts and paleoseismic recurrence intervals (e.g., Field, 2007; Grant and Lettis, 2003; Weldon et al., 2004, 2005). We assume that the amount of coseismic slip for each event is equal to the accumulated slip deficit on that segment. (3) Present-day crustal velocities are derived from 1709 GPS estimates from EarthScope PBO, as well as campaign GPS compiled by Corne Kreemer (Kreemer et al., 2009). An iterative least squares approach is used to adjust the locking depth along each segment. For this model, we included interseismic slip on 41 fault segments over variable locking depths (ranging from 1 to 23 km), and assume the following model parameters: shear modulus (30 GPa), mantle viscosity (1e19 Pa s) and elastic plate thickness (60 km). Best-fit models have an RMS residual velocity misfit of 2.02 mm/yr in the E–W direction, 2.69 mm/yr in the N–S direction and 2.73 mm/yr in the vertical direction.

Since the dislocation model with over 45 parameters cannot capture all of the tectonic and non-tectonic motions, especially in areas away from model fault segments, we fit the horizontal GPS residuals (using a 40 km block median) to a biharmonic spline using a tension factor of 0.45 (Wessel and Bercovici, 1998) weighted by the uncertainty in each GPS data point. The spline represents unmodeled fault motion at scales greater than 40 km wavelength. After fitting the residual GPS velocities, the horizontal data-model misfits are 1.47 mm/yr in the E–W direction and 1.56 mm/yr in the N–S direction.

References

Agnew, D.C., Owen, S., Shen, Z.K., Anderson, G., Svarc, J., Johnson, H., Austin, K.E., Reilinger, R. Coseismic displacements from the Hector Mine, California, earthquake: results from survey-mode GPS measurements. Bull. Seismol. Soc. Am. 92, 1355–1364, 2002.

Becker, T.W., Hardebeck, J.L., Anderson, G. Constraints on fault slip rates of the southern California plate boundary from GPS velocity and stress inversions. Geophys. J. Int. 160, 634–650, 2005.

Bennett, R.A., Rodi, W., Reilinger, R.E. Global Positioning System constraints on fault slip rates in southern California and northern Baja, Mexico. J. Geophys. Res. 101, 21943–21960, 1996.

Burgmann, R., Rosen, P.A., Fielding, E.J. Synthetic aperture radar interferometry to measure Earth's surface topography and its deformation. Annu. Rev. Earth Planet. Sci. 28, 169–209, 2000.

Doin, M.P., Lasserre, C., Peltzer, G., Cavalie, O., Doubre, C. Corrections of stratified tropospheric delays in SAR interferometry: validation with global atmospheric models. J. Appl. Geophys. 69, 35–50, 2009.

Elliott, J.R., Biggs, J., Parsons, B., Wright, T.J. InSAR slip rate determination on the Altyn Tagh Fault, northern Tibet, in the presence of topographically correlated atmospheric delays. Geophys. Res. Lett 35, L12309, 2008.

Emardson, T.R., Simons, M., Webb, F.H. Neutral atmospheric delay in interferometric synthetic aperture radar applications: statistical description and mitigation. J. Geophys. Res 108, 2231, 2003.

Fay, N.P., Humphreys, E.D. Fault slip rates, effects of elastic heterogeneity on geodetic data, and the strength of the lower crust in the Salton Trough region, southern California. J. Geophys. Res 9, 110, 2005.

Feigl, K.L., Agnew, D.C., Bock, Y., Dong, D., Donnellan, A., Hager, B.H., Herring, T.A., Jackson, D.D., Jordan, T.H., King, R.W. Space geodetic measurement of crustal deformation in central and southern California, 1984–1992. J. Geophys. Res. 98, 21677–21712, 1993.

Ferretti, A., Prati, C., Rocca, F. Nonlinear subsidence rate estimation using permanent scatterers in differential SAR interferometry. IEEE Trans. Geosci. Remote Sensing 38, 2202–2212, 2000.

Ferretti, A., Prati, C., Rocca, F. Permanent scatterers in SAR interferometry. IEEE Trans. Geosci. Remote Sensing 39, 8–20, 2001.

Fialko, Y. Evidence of fluid-filled upper crust from observations of postseismic deformation due to the 1992 Mw7. 3 Landers earthquake. J. Geophys. Res. 109, B08401, 2004a.

Fialko, Y. Probing the mechanical properties of seismically active crust with space geodesy: study of the coseismic deformation due to the 1992 Mw 7.3 Landers (southern California) earthquake. J. Geophys. Res. 109, B03307, 2004b.

Fialko, Y. Interseismic strain accumulation and the earthquake potential on the southern San Andreas fault system. Nature 441, 968–971, 2006.

Please cite this article in press as: Wei, M., et al. Optimal combination of InSAR and GPS for measuring interseismic crustal deformation. J. Adv. Space Res. (2010), doi:10.1016/j.asr.2010.03.013

Field, E.H. A summary of previous working-groups on California earthquake probabilities. B. Seismol. Soc. Am. 97 (4), 1033–1053, doi:10.1785/0120060048, 2007.

Freymueller, J.T., Murray, M.H., Segall, P., Castillo, D. Kinematics of the Pacific North America plate boundary zone, northern California, J. Geophys. Res. 104, 7419–7441, 1999.

Goldstein, R. Atmospheric limitations to repeat-track radar interferometry. Geophys. Res. Lett. 22 (18), 2517–2520, 1995.

Goldstein, R.M., Werner, C.L. Radar interferogram filtering for geophysical applications. Geophys. Res. Lett. 25, 4035–4038, 1998.

Gourmelen, N., Amelung, F., Casu, F., et al. Mining-related ground deformation in Crescent Valley, Nevada: implications for sparse GPS networks. Geophys. Res. Lett. 34, L09309, doi:10.1029/2007GL029427, 2007.

Hanssen, R.F. Radar Interferometry: Data Interpretation and Error Analysis. Kluwer Academic Publishers, Dordrecht, 2001.

Jin, S.G., Park, P.H. Strain accumulation in South Korea inferred from GPS measurements. Earth Planets Space 58 (5), 529–534, 2006.

Jin, S.G., Park, P.H., Zhu, W. Micro-plate tectonics and kinematics in Northeast Asia inferred from a dense set of GPS observations. Earth Planet. Sci. Lett. 257, 486–496, doi:10.1016/j.epsl.2007.03.0112007, 2007.

Johanson, I.A., Fielding, E.J., Rolandone, F., Burgmann, R. Coseismic and postseismic slip of the 2004 Parkfield earthquake from space-geodetic data. Bull. Seismol. Soc. Am. 96, 269–282, 2006.

Jonsson, S., Zebker, H., Segall, P., Amelung, F. Fault slip distribution of the 1999 Mw 7.1 Hector Mine, California, earthquake, estimated from satellite radar and GPS measurements. Bull. Seismol. Soc. Am. 92, 1377–1389, 2002.

Kreemer, C., Blewitt, G., Hammond, W.C., Plag, H.A. High-resolution strain rate tensor model for the Western U.S., Presentation at the EarthScope Annual Meeting, Boise, Idaho, 2009.

Li, Z., Fielding, E.J., Cross, P., Muller, J.P. Interferometric synthetic aperture radar atmospheric correction: medium resolution imaging spectrometer and advanced synthetic aperture radar integration. Geophys. Res. Lett. 33, doi:10.1029/2005GL025299, 2006.

Lohman, R.B., Simons, M. Some thoughts on the use of InSAR data to constrain models of surface deformation: noise structure and data downsampling. Geochem. Geophys. Geosyst. 6, Q01007, 2005.

Lyons, S., Sandwell, D. Fault creep along the southern San Andreas from interferometric synthetic aperture radar, permanent scatterers, and stacking. J. Geophys. Res. 108 (B1), 2047, doi:10.1029/2002JB001831, 2003.

Massonnet, D., Feigl, K., Rossi, M., Adragna, F. Radar interferometric mapping of deformation in the year after the Landers earthquake. Nature 369, 227–230, 1994.

Massonnet, D., Feigl, K.L. Radar interferometry and its application to changes in the Earth's surface. Rev. Geophys. 36, 441–500, 1998.

Massonnet, D., Rossi, M., Carmona, C., Adragna, F., Peltzer, G., Feigl, K., Rabaute, T. The displacement field of the Landers earthquake mapped by radar interferometry. Nature 364, 138–142, 1993.

Massonnet, D., Thatcher, W., Vadon, H. Detection of postseismic fault-zone collapse following the Landers earthquake. Nature 382, 612–616, 1996.

Meade, B.J., Hager, B.H. Block models of crustal motion in southern California constrained by GPS measurements. J. Geophys. Res. 110, B03403, 2005.

Mesinger, F., DiMego, G., Kalnay, K., et al. North American regional reanalysis. Bull. Am. Meteorol. Soc. 87, 343–360, 2006.

Payne, S.J., McCaffrey, R., King, R.W. Strain rates and contemporary deformation in the Snake River Plain and surrounding Basin and Range from GPS and seismicity. Geology 36, 647–650, 2008.

Peltzer, G., Crampe, F., Hensley, S., Rosen, P. Transient strain accumulation and fault interaction in the eastern California shear zone. Geol. Soc. Am. 29, 975–978, doi:10.1130/0091-7613(2001)029<0975:TSA-AFI>2.0.CO;2, 2001.

Peltzer, G., Hudnut, K.W., Feigl, K.L. Analysis of coseismic surface displacement gradients using radar interferometry: new insights into the Landers earthquake. J. Geophys. Res. 99, 21971–21981, 1994.

Peltzer, G., Rosen, P., Rogez, F., Hudnut, K. Postseismic rebound in fault step-overs caused by pore fluid flow. Science 273, 1202, 1996.

Pollitz, F.F., Wicks, C., Thatcher, W. Mantle flow beneath a continental strike-slip fault: postseismic deformation after the 1999 Hector Mine earthquake. Science 293 (5536), 1814–1818, 2001.

Rosen, P.A., Hensley, S., Joughin, I.R., Li, F.K., Madsen, S.N., Rodriguez, E., Goldstein, R.M. Synthetic aperture radar interferometry. Proc. IEEE 88, 333–382, 2000.

Rotta, H., Naglerb, T. The contribution of radar interferometry to the assessment of landslide hazards. Adv. Space Sci. 37, 710–719, 2006.

Sandwell, D.T., Bird, P., Freed, A., et al. Comparison of strain-rate maps of western North America, Presentation at the EarthScope Annual Meeting, Boise, Idaho, 2009.

Sandwell, D.T., Myer, D., Mellors, R., Shimada, M. Accuracy and resolution of ALOS interferometry: vector deformation maps of the father's day intrusion at Kilauea. IEEE Trans. Geosci. Remote Sensing 46, 3524–3534, 2008.

Sandwell, D.T., Price, E.J. Phase gradient approach to stacking interferograms. J. Geophys. Res. 103, 30183–30204, 1998.

Sandwell, D.T., Sichoix, L., Agnew, D., Bock, Y., Minster, J.B. Near real-time radar interferometry of the Mw 7.1 Hector Mine Earthquake. Geophys. Res. Lett. 27, 3101–3104, 2000.

Schmidt, D.A., Bürgmann, R. Time-dependent land uplift and subsidence in the Santa Clara valley, California, from a large interferometric synthetic aperture radar data set. J. Geophys. Res. 108, 2416, 2003.

Schmidt, D.A., Burgmann, R., Nadeau, R.M. Distribution of aseismic slip rate on the Hayward fault inferred from seismic and geodetic data. J. Geophys. Res 110, B08406, 2005.

Segall, P., Davis, J.L. GPS applications for geodynamics and earthquake studies. Annu. Rev. Earth Planet. Sci. 25, 301–336, 1997.

Simons, M., Fialko, Y., Rivera, L. Coseismic deformation from the 1999 Mw 7.1 Hector Mine, California, earthquake as inferred from InSAR and GPS observations. Bull. Seismol. Soc. Am. 92, 1390–1402, 2002.

Smith, B., Sandwell, D. Coulomb stress accumulation along the San Andreas Fault system. J. Geophys. Res. 108, 2296, 2003.

Smith, B.R., Sandwell, D.T. A model of the earthquake cycle along the San Andreas Fault System for the past 1000 years. J. Geophys. Res. 111, B01405, 2006.

Smith-Konter, B., Sandwell, D.T. Stress evolution of the San Andreas Fault system: recurrence interval vs. locking depth. Geophys. Res. Lett. 36, doi:10.1029/2009GL037235, 2009.

Smith-Konter, B., Solis, T., Sandwell, D.T. Data-derived stress uncertainties of the San Andreas Fault System. EOS Trans. AGU 89 (53), Fall Meet. Suppl., U51B-0029, 2008.

Sugaa, Y., Takeuchia, S., Oguroa, Y., et al. Application of ERS-2/SAR data for the 1999 Taiwan earthquake. Adv. Space Sci. 28, 155–163, 2001.

Tomiyama, N., Koike, K., Omura, M. Detection of topographic changes associated with volcanic activities of Mt. Hossho using D-InSAR. Adv. Space Sci. 33, 279–283, 2004.

Tong, X., Sandwell, D.T., Fialko, Y. Coseismic slip model of the 2008 Wenchuan earthquake derived from joint inversion of interferometric synthetic aperture radar, GPS, and field data. J. Geophys. Res., doi:10.1029/2009JB006625, 2010.

Uppala, S., Kållberg, P., Simmons, A., Andrae, U. The ERA-40 re-analysis. Q. J. R. Meteorol. Soc 131, 2961–3012, 2005.

Wdowinski, S., Smith-Konter, B., Bock, Y., Sandwell, D.T. Spatial characterization of the interseismic velocity field in southern California. Geology 35, 311–314, 2007.

Wei, M., Sandwell, D. Decorrelation of L-band and C-band interferometry over vegetated areas in California. IEEE Trans. Geosci. Remote Sensing, in press, 2010.

Wei, M., Sandwell, D., Fialko, Y. A silent Mw 4.7 slip event of October 2006 on the Superstition Hills fault, southern California. J. Geophys. Res. 114, B07402, 2009.

Please cite this article in press as: Wei, M., et al. Optimal combination of InSAR and GPS for measuring interseismic crustal deformation. J. Adv. Space Res. (2010), doi:10.1016/j.asr.2010.03.013

Wessel, P., Bercovici, D. Interpolation with splines in tension: a green's function approach. Math. Geol. 30 (1), 77–93, 1998.

Wright, T.J., Parsons, B., England, P.C., Fielding, E.J. InSAR observations of low slip rates on the major faults of Western Tibet. Science 305, 236–239, 2004.

Zebker, H.A., Rosen, P. Atmospheric artifacts in interferometric SAR surface deformation and topographic maps. J. Geophys. Res. 102, 7547–7563, 1997.

Zebker, H.A., Rosen, P., Goldstein, R., Gabriel, A., Werner, C.L. On the derivation of coseismic displacement fields using differential radar interferometry: the Landers earthquake, in: Geoscience and Remote Sensing Symposium, 1994. IGARSS'94. Surface and Atmospheric Remote Sensing: Technologies, Data Analysis and Interpretation, International, 1, 1994.

Please cite this article in press as: Wei, M., et al. Optimal combination of InSAR and GPS for measuring interseismic crustal deformation. J. Adv. Space Res. (2010), doi:10.1016/j.asr.2010.03.013